SCIENTIFIC REPORTS

OPEN

Received: 15 September 2016
Accepted: 23 January 2017
Published: 27 February 2017

Thermoelectric SnS and SnS-SnSe solid solutions prepared by mechanical alloying and spark plasma sintering: Anisotropic thermoelectric properties

Asfandiyar[1], Tian-Ran Wei[1], Zhiliang Li[1], Fu-Hua Sun[1], Yu Pan[1], Chao-Feng Wu[1], Muhammad Umer Farooq[2], Huaichao Tang[1], Fu Li[3,4], Bo Li[3] & Jing-Feng Li[1]

***P*–type SnS compound and $SnS_{1-x}Se_x$ solid solutions were prepared by mechanical alloying followed by spark plasma sintering (SPS) and their thermoelectric properties were then studied in different compositions (x = 0.0, 0.2, 0.5, 0.8) along the directions parallel (//) and perpendicular (⊥) to the SPS–pressurizing direction in the temperature range 323–823 K. SnS compound and $SnS_{1-x}Se_x$ solid solutions exhibited anisotropic thermoelectric performance and showed higher power factor and thermal conductivity along the direction ⊥ than the // one. The thermal conductivity decreased with increasing contents of Se and fell to 0.36 W m^{-1} K^{-1} at 823 K for the composition $SnS_{0.5}Se_{0.5}$. With increasing selenium content (x) the formation of solid solutions substantially improved the electrical conductivity due to the increased carrier concentration. Hence, the optimized power factor and reduced thermal conductivity resulted in a maximum *ZT* value of 0.64 at 823 K for $SnS_{0.2}Se_{0.8}$ along the parallel direction.**

Thermoelectric (TE) devices have the ability to convert waste heat directly into electrical energy and vice versa, which have advantages of no moving parts, no emission of any greenhouse gases, quiet operation, being free from liquid fuels and high reliability[1]. The conversion efficiency of thermoelectric devices can be characterized by the dimensionless figure of merit, $ZT = S^2\sigma T/\kappa$ where the parameters S is the Seebeck coefficient, σ is the electrical conductivity, κ is the thermal conductivity which consists of the lattice conductivity (κ_L) and the electronic thermal conductivity (κ_e) and T is the absolute temperature[2].

SnS and SnSe have received increasing attention as new thermoelectric materials with abundant resources and better environmental compatibility[3,4]. These materials in their pristine form possess high Seebeck coefficient and low thermal conductivity but low electrical conductivity due to the low carrier concentration which results in low *ZT* values. Electrical conductivity can be enhanced by optimizing carrier concentration through elemental doping and band convergence[5–10], while thermal conductivity can be suppressed *via* forming solid solutions (alloying)[11,12], nanostructure architecture and microstructure modulation[13–19] by virtue of intensifying phonon scattering at atomic, nano and micro scales, respectively. Among these strategies, forming solid solutions[20–23] has also been revealed as an effective way to modify the band structures: it can alter the band shape[24] (effective mass), change the band gap[25] (related to bipolar effect), and also affect the relative position of different bands[10,26] (band alignment and convergence), thus directly determining charge transport and thermoelectric performance. Recently a *ZT* value up to 0.6 at 873 K was achieved in Ag–doped SnS polycrystals by Tan *et al.*[4], which is 275% higher than the undoped samples[11,27]. SnSe is the heavier analogue of SnS, and both crystalize in

[1]State Key Laboratory of New Ceramics and Fine Processing, School of Material Science and Engineering, Tsinghua University, Beijing 100084, China. [2]Xinjiang Inspection Institute of Special Equipment, Urumqi, 830011, China. [3]Advanced Materials Institute, Graduate School at Shenzhen, Tsinghua University, Shenzhen, 518055, China. [4]School of Physics and Energy, and Shenzhen Key Laboratory of Sensor Technology, Shenzhen University, Shenzhen, 518060, China. Correspondence and requests for materials should be addressed to J.-F.Li. (email: jingfeng@mail.tsinghua.edu.cn) or Z.L.Li. (email: 460407475@qq.com)

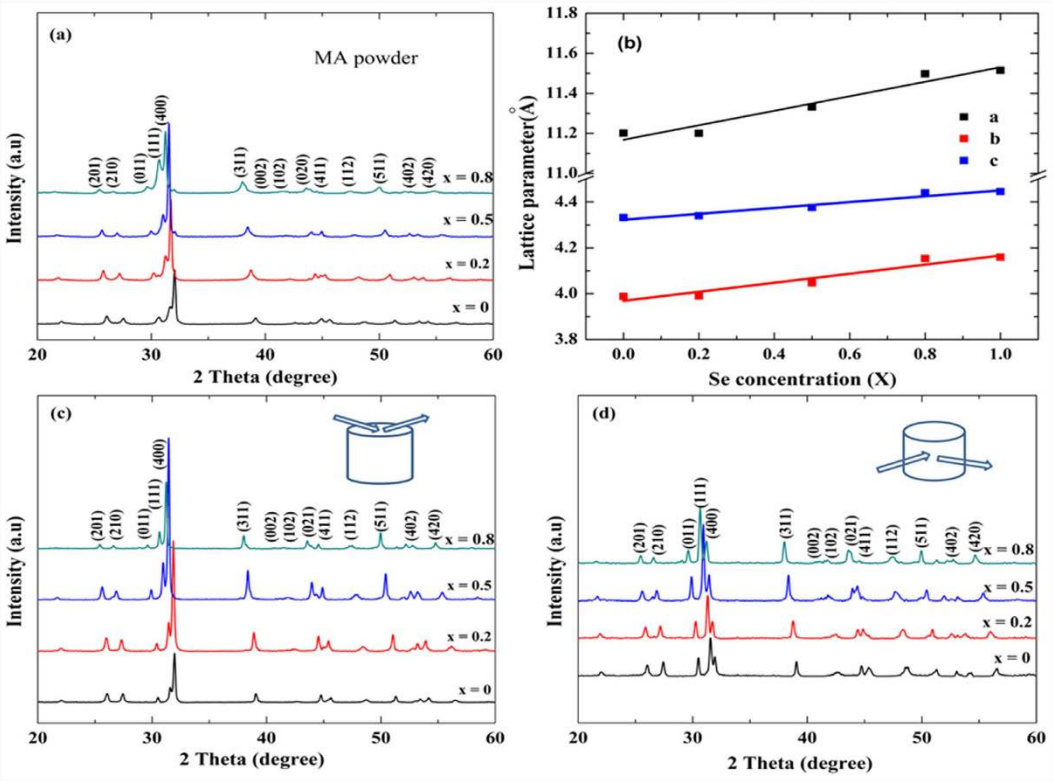

Figure 1. (**a**) XRD patterns of $SnS_{1-x}Se_x$ (x = 0, 0.2, 0.5, 0.8) MA–powders. (**b**) Lattice parameters of $SnS_{1-x}Se_x$ solid solutions varying with the increase in Se content (x). (**c,d**) XRD patterns of $SnS_{1-x}Se_x$ bulk specimens cut along two different directions.

highly anisotropic layered orthorhombic structure (*Pnma*) at room temperature and convert to *Cmcm* at high temperatures[3,9,11]. Optical properties on the two materials has been studied extensively in the past[28,29], and recent attention has been paid to their thermoelectric properties[3,4,9,13,19]. Guo *et al.*[30] comparatively calculated the *ZT* values of SnSe and SnS using first principle and the Boltzmann transport, and found that SnSe has larger optimal *ZT* than SnS. Recently an unprecedented *ZT* of 2.6 at 973 K was observed in SnSe single crystal along *b*–axis due to moderate power factor and ultra–low lattice thermal conductivity[3]. Nevertheless, due to the rigorous and low–efficiency of synthetic process of the single crystals, most of the thermoelectric materials are expected to work in polycrystalline forms, which can be synthesized through low cost powder metallurgical processes. A typical example is a combination of mechanical alloying (MA) and spark plasma sintering (SPS). The advantage of MA is to get fine powders in a short alloying time and low fabrication cost while SPS treatment can achieve high density close to the theoretical value and keeps the original microstructure using faster rate which also help to avoid the coarsening of grains.

In this work $SnS_{1-x}Se_x$ solid solutions with different x values were obtained by MA combined with SPS. Although relatively low thermal conductivity was achieved in the composition $SnS_{0.5}Se_{0.5}$ rather than $SnS_{0.2}Se_{0.8}$ that was reported previously[11], the power factor ($PF = S^2\sigma$) was greatly optimized in the composition $SnS_{0.2}Se_{0.8}$ than in the composition $SnS_{0.5}Se_{0.5}$. Hence, the optimized power factor along with reduce thermal conductivity resulted in a high *ZT* value of 0.64 at 823 K for $SnS_{0.2}Se_{0.8}$ without doping along the direction parallel to the SPS–pressurizing direction.

Results and Discussion

Phase and microstructure. SnS and SnSe compounds are crystallized in a layered structure with orthorhombic *Pnma* space group (PDF#39–0354 and PDF#48–1224) at room temperature and show a phase transition from *Pnma* to the *Cmcm* symmetry at high temperatures (858 K for SnS and 803 K for SnSe)[3–5]. Figure 1 represents the XRD patterns of the pure SnS and $SnS_{1-x}Se_x$ solid–solution powders and bulk samples along two different directions. The result confirms that single–phase $SnS_{1-x}Se_x$ solid solutions with an orthorhombic crystal structure were formed. A shift in 2θ of all peaks toward the lower angle was observed with increasing x. The lattice parameters of $SnS_{1-x}Se_x$ solid solution powders expand linearly with increase in Se contents (x), which are in accordance with the Vegard's law (Fig. 1b), indicating that the smaller S atoms were replaced by the larger Se. Obvious anisotropy is seen from the XRD patterns of the bulk specimens cut along the two directions. For the specimen cut perpendicular to the SPS pressure (specimen$_\perp$, Fig. 1c), (400) peak is much stronger than the specimen$_{//}$ (Fig. 1d). In fact, the calculated orientation factors of (400) are 0.3 and 0.13 for specimen$_\perp$ and specimen$_{//}$, respectively. This anisotropy has been widely observed and explained in previous studies on polycrystalline SnS, SnSe and other layered compounds[3,11]. From the FESEM images we can see an obvious thin–platelet morphology

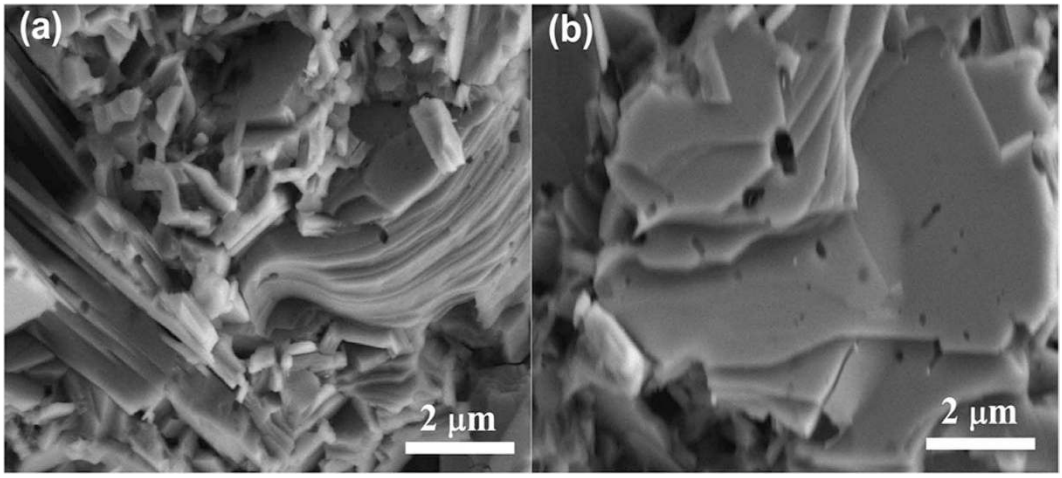

Figure 2. FESEM morphology of fractured surfaces of SnS bulk sample (**a**) parallel (//) and (**b**) perpendicular (⊥) to the SPS–pressurizing direction.

Se content (x)	0	0.2	0.5	0.8
Nominal comp %	50:50	50:40:10	50:25:25	50:10:40
Real comp %	51.3:48.7	51.7:38.7:9.60	51.1:24.3:24.6	50.6:10.5:38.8
Density (g/cm^3)	4.97	5.17	5.32	5.45

Table 1. Nominal composition, real composition and density of $SnS_{1-x}Se_x$ at room temperature.

(Fig. 2a,b). The cross-section$_\perp$ shows a flat surface (parallel to the (400) crystallographic plane) of platelets compare to other directions, which is in good agreement with the anisotropic XRD patterns shown in Fig. 1c and d. Inside the grains pores are present with relative densities ranging from 96.3% to 91.2%. This phenomenon is possibly related to the slight volatilization of S and Se that is also seen from the composition detected by ICP shown in Table 1.

Electrical transport. The Seebeck coefficient (S) of $SnS_{1-x}Se_x$ solid solutions as a function of temperature along two directions is shown in Fig. 3. $S_\perp$ is 352 μV/K at 323 K, which is well consistent with our previous reports[4,27] but somewhat lower than the data reported by Han *et al.*[11] In fact, over the whole temperature range, $S_{//}$, $S_\perp$ value of SnS (this work) and $S_\perp$ in our previous work[4,27] are lower than the published data[11]. The difference in the S values probably originates from the synthesis processes of the samples (mechanical alloying, SPS and melting, SPS). Similar difference also exists in the S value of SnSe prepared by different methods[10,31]. S decreases with increase in Se contents (x) due to the increased carrier concentration as well as slightly enhanced mobility (as shown in Table 2). S along both directions of all the samples increases in the temperature range 323–673 K and then turns to decrease with increasing temperature due to bipolar conduction. It is also seen that $S_\perp$ is lower than $S_{//}$ for all the compositions over the whole temperature range.

Figure 3(c) and (d) shows the electrical conductivity (σ) of $SnS_{1-x}Se_x$ solid solutions in the temperature range 323–823 K in the two directions. The σ of the $SnS_{1-x}Se_x$ solid solutions increases with rising temperature. $\sigma_\perp$ of SnS is 3.24×10^{-3} S/cm at 323 K, which is comparable to our previous studies[4,27] but greatly lower than Han's work[11]. For solid solutions, σ is also lower than the same composition in ref. 11. This phenomenon is ascribed to the lower carrier concentration (n_H) and mobility (μ_H) in this work as shown in Table 2. The lower mobility can be intuitively understood since samples here prepared by MA should contain abundant defects that act as scattering centers of carriers. The reason for the lower carrier concentration is not quite clear. We tentatively argue that the off stoichiometry, probably the existence of S deficiencies, may be important. Recalling the Seebeck coefficient as mentioned above, it is also smaller in this study, which seems to be in contrary to the common sense that a lower n_H usually gives a larger S. However, this simple prediction is reliable only when the dominant scattering mechanisms are similar, which need further investigation. σ decreases with increase of Se content (x) for $x = 0.2$ at 323 K, which is due to the impaired carrier mobility by alloying. With even more Se, σ increases with x, which is mainly due to increased n_H. It is also seen that over the whole temperature range all the $SnS_{1-x}Se_x$ solid solutions, $\sigma_{//}$ is lower than $\sigma_\perp$ one due to the preferred orientation of the (400) plane in this direction, which is related to the larger effective mass and the consequentially lower carrier mobility along this direction[3]. The highest electrical conductivities of 33.1 S/cm and 27 S/cm are obtained at 823 K for the composition $SnS_{0.2}Se_{0.8}$ along the directions ⊥ and // to the SPS–pressurizing direction, respectively. Figure 3(e) and (f) present the power factors ($PF = S^2\sigma$) of all the $SnS_{1-x}Se_x$ samples versus selenium content (x). Over the entire temperature range, the $PF_\perp$ is higher than $PF_{//}$. The maximum $PF_\perp$ and $PF_{//}$ of the composition $SnS_{0.2}Se_{0.8}$ at 823 K are 3.7 μW cm^{-1} K^{-2} and 2.93 μW cm^{-1} K^{-2}, respectively.

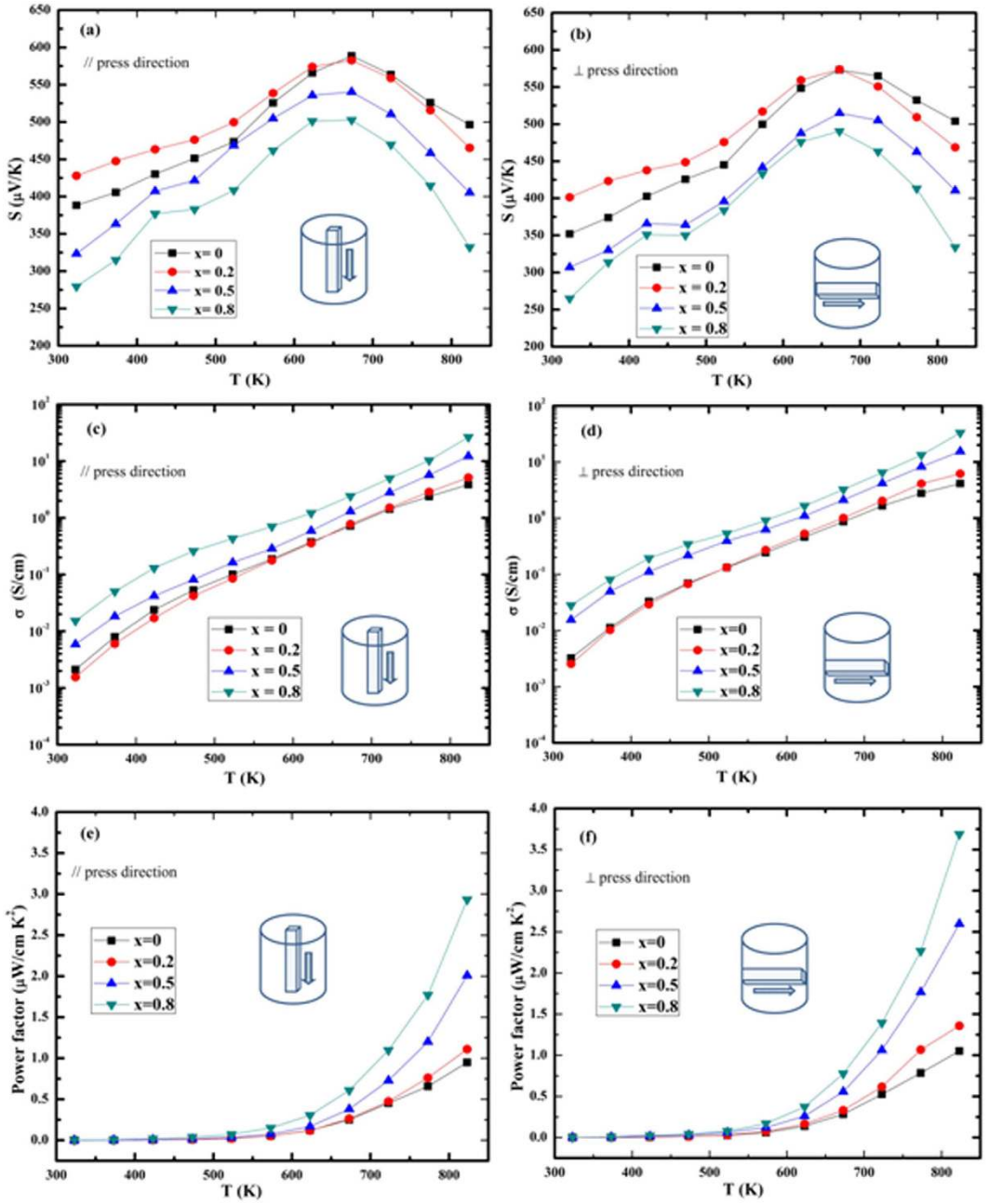

Figure 3. Temperature dependence of the (**a,b**) Seebeck coefficient, (**c,d**) electrical conductivity and (**e,f**) power factor of the $SnS_{1-x}Se_x$ (x = 0, 0.2, 0.5, 0.8) solid solutions (**a,c,e**) along and (**b,d,f**) perpendicular to the SPS-pressurizing direction.

Measured Parameters	Se concentration (x)			
	x = 0	x = 0.2	x = 0.5	x = 0.8
n_H (⊥) (10^{17} cm^{-3})	0.00902	0.505	1.12	2.10
μ_H (⊥) (cm^2/Vs)	7.32	0.523	0.438	0.645
$S_{//}$ (μV/K)	388	428	323	279
$S_{\perp}$ (μV/K)	352	401	307	265
$\sigma_{//}$ (S/m)	0.211	0.155	0.588	1.53
$\sigma_{\perp}$ (S/m)	0.324	0.255	1.55	2.80

Table 2. Carrier concentration and mobility of $SnS_{1-x}Se_x$ measured on the specimens cut perpendicular to the SPS pressurizing direction (⊥, in-plane measurement) at room temperature and Seebeck coefficient and electrical conductivity along (//) and (⊥) directions obtained at 323 K.

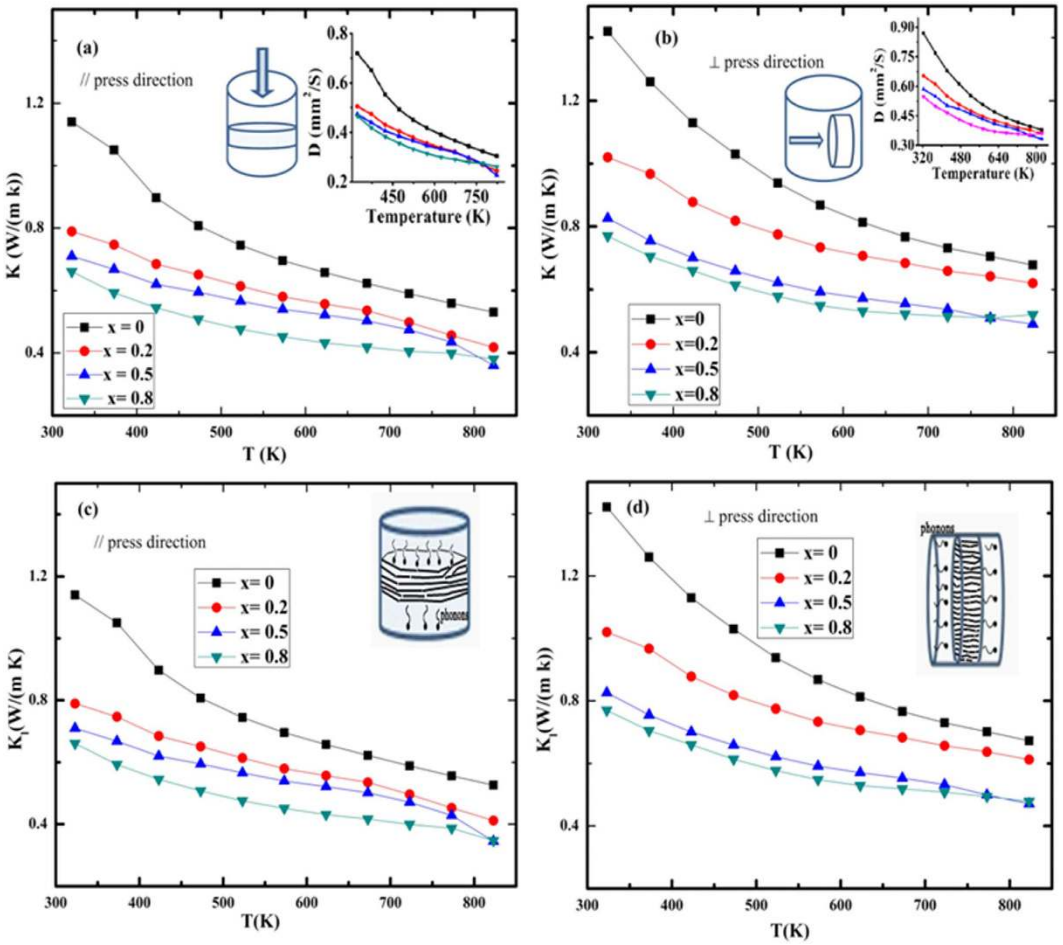

Figure 4. Temperature dependence of the total thermal conductivity (the inset shows the thermal diffusivity) of the $SnS_{1-x}Se_x$ (x = 0, 0.2, 0.5, 0.8) solid solutions (**a**) parallel (//) and (**b**) perpendicular (⊥) to the SPS–pressurizing direction. The lattice thermal conductivity of the $SnS_{1-x}Se_x$ solid solution (**c**) parallel (//) and (**d**) perpendicular (⊥) to the SPS–pressurizing direction.

Thermal transport. The temperature dependence of total thermal conductivity (κ) and lattice thermal conductivity (κ_L) of the $SnS_{1-x}Se_x$ solid solutions is shown in Fig. 4. Inset of Fig. 4(a) and (b) represents the thermal diffusivity along the // and ⊥ directions. Over the whole temperature range, $\kappa_{//}$ of all the samples are lower than the $\kappa_{\perp}$. κ decreased with x and the lowest value 0.36 $W\,m^{-1}\,K^{-1}$ at 823 K was obtained for $SnS_{0.5}Se_{0.5}$ along the // direction. For all the $SnS_{1-x}Se_x$ samples κ decreases with increasing temperature. For x = 0.5 κ decreases faster above 773 K than for x = 0.8, which leads to the lower κ in the $SnS_{0.5}Se_{0.5}$ composition. Similar behavior for this composition has also been found in Han's work[11], but the reason is still unclear. κ and κ_L of polycrystalline SnS compound along the direction ⊥ to the SPS–pressurizing direction are all 1.4 $W\,m^{-1}\,K^{-1}$ which is consistent with the previously reported value for SnS compound measured along the same direction[4]. κ_L decreases with increase of selenium content (x) due to the alloying effect caused by different atomic masses of Se (79.86 g/mol) and S (32.07 g/mol) and strain field fluctuation caused by difference in atomic radii (1.91 Å of Se and 1.84 Å of S). κ_l decreases with increasing temperature for all the $SnS_{1-x}Se_x$ samples due to the intensified Umklapp process. Due to the anisotropy in microstructure, $\kappa_{//}$ is considerably lower than $\kappa_{\perp}$.

Figure of merit (*ZT*). The *ZT* values of all the $SnS_{1-x}Se_x$ (x = 0, 0.2, 0.5, 0.8) solid solutions along the directions // and ⊥ to the SPS–pressurizing one were calculated from the combination of anisotropic electrical and thermal transport properties (Fig. 5). Over the whole temperature range, $ZT_{//}$ values were higher than $ZT_{\perp}$, which comes mainly from the greatly suppressed thermal conductivity although power factors are lower along this direction. $ZT_{//}$ for SnS is 0.15 at 823 K and increases with Se content. The *ZT* values of all the $SnS_{1-x}Se_x$ samples increased rapidly with rising temperature and a maximum value of 0.64 at 823 K for composition $SnS_{0.2}Se_{0.8}$ was obtained along the direction // to the SPS–pressurizing direction.

Conclusion

P–type SnS compound and $SnS_{1-x}Se_x$ solid solutions were successfully prepared by mechanical alloying combined with spark plasma sintering. High anisotropy among all the transport properties has been observed, *i.e.* higher *PF* and σ along the direction perpendicular to the SPS–pressurizing direction than the parallel one. Se substitution

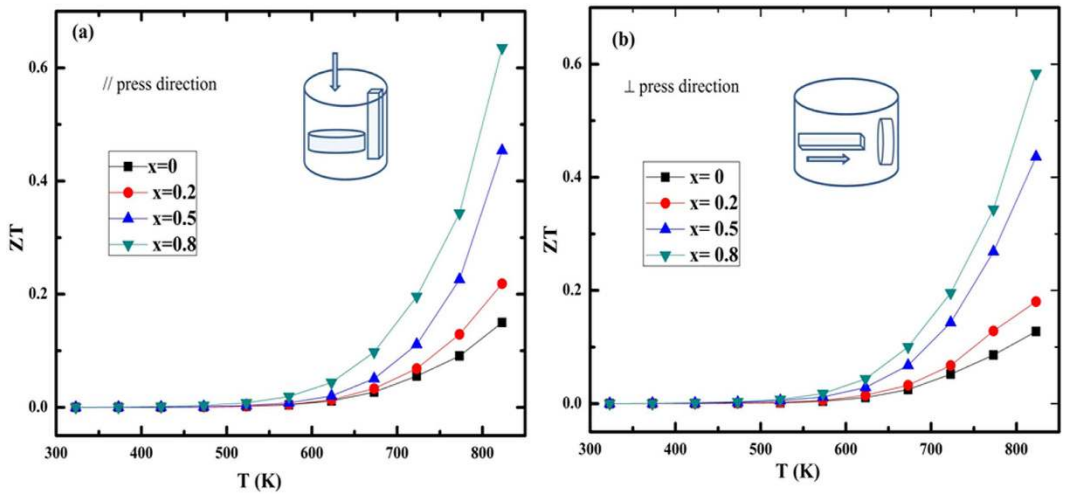

Figure 5. Temperature dependence of the *ZT* values of $SnS_{1-x}Se_x$ (x = 0, 0.2, 0.5, 0.8) solid solutions (**a**) parallel (//) and (**b**) perpendicular (⊥) to the SPS–pressurizing direction.

subsequently increased the hole carrier concentration from $9.02 \times 10^{14}\,cm^{-3}$ in SnS to $2.10 \times 10^{17}\,cm^{-3}$ in $SnS_{0.2}Se_{0.8}$, which results in increased σ and *PF*. A high *ZT* value of 0.64 has been obtained for the composition $SnS_{0.2}Se_{0.8}$ at 823 K along the direction // to the SPS–pressuring direction due to the reduced κ and optimized *PF*. SnS and all the $SnS_{1-x}Se_x$ solid solutions exhibit higher thermoelectric performance along the direction parallel to the SPS–pressurizing direction than the other one. Moreover, although a low κ of 0.36 at 823 K was observed in $SnS_{0.5}Se_{0.5}$, its maximum *ZT* value 0.45 is still lower than the $SnS_{0.2}Se_{0.8}$ owing to its low σ and *PF*. However, both compositions ($SnS_{0.5}Se_{0.5}$, $SnS_{0.2}Se_{0.8}$) are promising candidates for further thermoelectric investigations towards higher performance through proper *p*–type doping to increase σ and *PF*.

Materials and Methods

Materials. The experiments started from raw elements Sn (99.99% powder), S (99.99% shots) and Se (99.9% powder). The raw materials with a total mass of 20 g were weighed according to the nominal compositions of $SnS_{1-x}Se_x$ (x = 0, 0.2, 0.5, 0.8), loaded into a stainless steel jar of volume 250 ml with stainless steel balls of different diameters and masses (10 mm, ~4 g and 6 mm, ~1 g) in a dry argon–filled glow box and then subjected to MA. The numbers of large and small balls were 44 and 250, respectively. Ball milling was conducted continuously at 450 rpm for 15 hours. The MA–derived powders were then loaded into a graphite die with an inner diameter of 15 mm and was spark plasma sintered at 903 K in vacuum for 7 min under axial pressure of 50 MPa. Finally, a cylinder shaped samples of average thickness about 12 mm and 15 mm in diameter were obtained. The phase structure of all the samples were examined by X–ray diffraction (XRD) using Cu Kα radiation (λ = 1.5418 Å). The morphology of the bulk samples was observed through a field emission scanning electron microscope (FE–SEM, JSM–7001 JEOL, Japan). The chemical composition was analyzed by inductively coupled plasma optical emission spectroscopy (ICP-OES, VISTA-MPX, Varian, USA). To investigate the electrical and thermal transport properties along the directions parallel and perpendicular to the SPS–pressurizing direction, bar–shaped specimens ($2 \times 2 \times 11$ mm) and disks ($\varphi 6 \times 1.2$ mm) were cut from bulk samples and polished with fine–grit sandpaper. The simultaneous measurement of the Seebeck coefficient and electrical resistivity was done using bar–shaped samples by a Seebeck coefficient/electrical measuring system (ZEM–2, ULVAK–RIKO, Japan), under partial helium pressure in the temperature range 323–823 K. The Hall coefficients were obtained at room temperature by the Van der Paw technique under a reversible magnetic field of 0.52 T (8340 DC, Toyo Japan). The density (*d*) of the bulk samples were measured by the Archimedes method. The C_P values of SnS and SnSe were obtained from previous work[3,32], and the values for solid solutions were calculated using linear average. The disk–shaped samples were used to measure the thermal diffusivity (*D*) by the laser flash model (TC–9000, ULVAC–RIKO Japan). The heat capacity and density of the $SnS_{1-x}Se_x$ samples can be found in Table S1 (Supplementary Information) and Table 1. Finally, the total thermal conductivity was calculated using $\kappa = DC_Pd$.

References

1. Snyder, G. J. & Toberer, E. S. Complex thermoelectric materials. *Nature Materials* **7,** 105–114 (2008).
2. Nolas, G. S., Sharp, J. & Goldsmid, J. *Thermoelectrics: basic principles and new materials developments*. Vol. 45 (Springer Science & Business Media, 2013).
3. Zhao, L.-D. *et al.* Ultralow thermal conductivity and high thermoelectric figure of merit in SnSe crystals. *Nature* **508,** 373–377 (2014).
4. Tan, Q. *et al.* Thermoelectrics with earth abundant elements: low thermal conductivity and high thermopower in doped SnS. *J. Mater. Chem. A.* **2,** 17302–17306 (2014).
5. Chen, C.-L., Wang, H., Chen, Y.-Y., Day, T. & Snyder, G. J. Thermoelectric properties of p-type polycrystalline SnSe doped with Ag. *J. Mater. Chem. A.* **2,** 11171–11176 (2014).
6. Sassi, S. *et al.* Assessment of the thermoelectric performance of polycrystalline p-type SnSe. *App. Phys. Lett.* **104,** 212105 (2014).
7. Chere, E. K. *et al.* Studies on thermoelectric figure of merit of Na-doped p-type polycrystalline SnSe. *J. Mater. Chem. A.* **4,** 1848–1854 (2016).

8. Pei, Y. *et al.* Convergence of electronic bands for high performance bulk thermoelectrics. *Nature* **473,** 66–69 (2011).
9. Zhao, L.-D. *et al.* Ultrahigh power factor and thermoelectric performance in hole-doped single-crystal SnSe. *Science* **351,** 141–144 (2016).
10. Wei, T.-R. *et al.* Distinct impact of alkali-ion doping on electrical transport properties of thermoelectric p-type polycrystalline SnSe. *J. Am. Chem. Soc.* **138,** 8875–8882 (2016).
11. Han, Y.-M. *et al.* Thermoelectric performance of SnS and SnS–SnSe solid solution. *J. Mater. Chem. A*. **3,** 4555–4559 (2015).
12. Wu, C.-F., Wei, T.-R. & Li, J.-F. Electrical and thermal transport properties of $Pb_{1-x}Sn_xSe$ solid solution thermoelectric materials. *Phys. Chem. Chem. Phys.* **17,** 13006–13012 (2015).
13. Zhao, L.-D. *et al.* Thermoelectrics with earth abundant elements: high performance p-type PbS nanostructured with SrS and CaS. *J. Am. Chem. Soc.* **134,** 7902–7912 (2012).
14. Zhai, Y. *et al.* Enhanced thermoelectric performance in n-type $Bi_2Te_{2.994}Cl_{0.006}/In_2Te_3$ composite. *J. Alloys Compd.* **563,** 285–288 (2013).
15. Zhai, Y. *et al.* Thermoelectric performance of the ordered In_4Se_3–In composite constructed by monotectic solidification. *J. Mater. Chem. A*. **1,** 8844–8847 (2013).
16. Ben-Yehuda, O., Shuker, R., Gelbstein, Y., Dashevsky, Z. & Dariel, M. Highly Textured Bi_2Te_3-based Materials For Thermoelectric Energy Conversion. *J. appl. phys.* **101,** 3707 (2007).
17. Mikami, M., Guilmeau, E., Funahashi, R., Chong, K. & Chateigner, D. Enhancement of electrical properties of the thermoelectric compound $Ca_3Co_4O_9$ through use of large-grained powder. *J. Mater. Res.* **20,** 2491–2497 (2005).
18. Popuri, S. *et al.* Large thermoelectric power factors and impact of texturing on the thermal conductivity in polycrystalline SnSe. *J. Mater. Chem. C.* **4,** 1685–1691 (2016).
19. Zhao, L.-D. *et al.* Enhanced thermoelectric properties in the counter-doped SnTe System with strained endotaxial SrTe. *J. Am. Chem. Soc.* **138,** 2366–2373 (2016).
20. Zaitsev, V. *et al.* Highly effective $Mg_2Si_{1-x}Sn_x$ thermoelectrics. *Phys. Rev. B* **74,** 045207 (2006).
21. Zhang, Q. *et al.* High figures of merit and natural nanostructures in $Mg_2Si_{0.4}Sn_{0.6}$ based thermoelectric materials. *App. Phys. Lett.* **93,** 102109 (2008).
22. Yan, X. *et al.* Experimental studies on anisotropic thermoelectric properties and structures of n-type $Bi_2Te_{2.7}Se_{0.3}$. *Nano Lett.* **10,** 3373–3378 (2010).
23. Xiao, Y. *et al.* Enhanced thermoelectric figure of merit in p-type $Bi_{0.48}Sb_{1.52}Te_3$ alloy with WSe_2 addition. *J. Mater. Chem. A*. **2,** 8512–8516 (2014).
24. Fu, T. *et al.* Enhanced thermoelectric performance of PbTe bulk materials with figure of merit $ZT > 2$ by multi-functional alloying. J. *Materiomics* **2,** 141–149 (2016).
25. Wang, H., LaLonde, A. D., Pei, Y. & Snyder, G. J. The criteria for beneficial disorder in thermoelectric solid solutions. *Adv. Funct. Mater.* **23,** 1586–1596 (2013).
26. Pei, Y., Heinz, N. A. & Snyder, G. J. Alloying to increase the band gap for improving thermoelectric properties of Ag_2 Te. *J. Mater. Chem*. **21,** 18256–18260 (2011).
27. Tan, Q. & Li, J.-F. Thermoelectric properties of Sn-S bulk materials prepared by mechanical alloying and spark plasma sintering. *J. Elec. Materi* **43,** 2435–2439 (2014).
28. Baumgardner, W. J., Choi, J. J., Lim, Y.-F. & Hanrath, T. SnSe nanocrystals: synthesis, structure, optical properties, and surface chemistry. *J. Am. Chem. Soc.* **132,** 9519–9521 (2010).
29. Vidal, J. *et al.* Band-structure, optical properties, and defect physics of the photovoltaic semiconductor SnS. *Appl. Phys. Lett.* **100,** 032104 (2012).
30. Guo, R., Wang, X., Kuang, Y. & Huang, B. First-principles study of anisotropic thermoelectric transport properties of IV-VI semiconductor compounds SnSe and SnS. *Phys. Rev. B* **92,** 115202 (2015).
31. Wei, T.-R. *et al.* Thermoelectric transport properties of pristine and Na-doped $SnSe_{1-x}Te_x$ polycrystals. *Phys. Chem. Chem. Phys.* **17,** 30102–30109 (2015).
32. Orr, R. L. & Christensen, A. High Temperature Heat Contenits of Stannous and Stannic Sulfides. *J. Phys. Chem.* **62,** 124–125 (1958).

Acknowledgements

This work was supported by the National Basic Research Program of China (Grant No. 2013CB632503) and the National Natural Science Foundation (No. 11474176) as well as The Science and Technology Plan of Shenzhen City under grant JCYJ20150827165038323.

Author Contributions

J.-F. Li and Asfandiyar designed the project, Asfandiyar performed part of the experiments and drafted the manuscript; Asfandiyar, T.-R. Wei and J.-F. Li revised the text; T.-R. Wei, Z. Li, F.-H. Sun, Y. Pan, C.-F. Wu, M.-U. Farooq, H. Tang, F. Li and B. Li helped in characterization and added their input in results & discussions.

Additional Information

Supplementary information accompanies this paper at http://www.nature.com/srep

Competing financial interests: The authors declare no competing financial interests.

How to cite this article: Asfandiyar *et al.* Thermoelectric SnS and SnS-SnSe solid solutions prepared by mechanical alloying and spark plasma sintering: Anisotropic thermoelectric properties *Sci. Rep.* **7**, 43262; doi: 10.1038/srep43262 (2017).